

Use of machine learning to improve simulations of climate

Janni Yuval¹ and Paul A. O’Gorman¹

¹Massachusetts Institute of Technology, Cambridge, Massachusetts
02139, USA

Global climate models represent small-scale processes such as clouds and convection using quasi-empirical models known as parameterizations, and these parameterizations are a leading cause of uncertainty in climate projections. A promising alternative approach is to use machine learning to build new parameterizations directly from high-resolution model output. However, parameterizations learned from three-dimensional model output have not yet been successfully used for simulations of climate. Here we use a random forest to learn a parameterization of subgrid processes from output of a three-dimensional high-resolution atmospheric model. Integrating this parameterization into the atmospheric model leads to stable simulations at coarse resolution that replicate the climate of the high-resolution simulation. The parameterization obeys physical constraints and captures important statistics such as precipitation extremes. The ability to learn from a fully three-dimensional simulation presents an opportunity for learning parameterizations from the wide range of global high-resolution simulations that are now emerging.

Coupled atmosphere-ocean simulations of climate typically resolve atmospheric processes on horizontal length scales of order 50-100km. Smaller-scale processes are represented by subgrid parameterizations schemes that frequently rely on heuristic arguments. Parameterizations are a main cause for the large uncertainty in temperature, precipitation and wind projections [1, 2, 3, 4, 5, 6]. Although increases in computational resources have now made it possible to run simulations of the atmosphere that resolve deep convection on global domains for periods of a month or more [7, 8], such simulations cannot be run for the much longer time scales over which the climate system responds to radiative forcing [9], and the computational cost to explicitly resolve important low cloud feedbacks will remain out of reach for the foreseeable future [6]. Therefore, novel and computationally efficient approaches to subgrid parameterization development are urgently needed and are at the forefront of climate research. Subgrid parameterizations that are trained using machine learning (ML) provide one possible route forward given the availability of high-resolution model output for use as training datasets [10, 11, 12, 13, 14, 15, 16]. Training on both the control climate and a warm climate is needed to simulate a warming climate using an ML parameterization [12, 13], and this is feasible because only a relatively short run of a high-resolution model is needed for training data in the warmer climate.

Recently a deep artificial neural network (NN) was successfully used to emulate the embedded two-dimensional cloud-system resolving model in a superparameterized climate model on an aquaplanet [11, 12], although some choices of NN architecture lead to blow ups in the simulations [17]. An NN parameterization has also been recently learned from the coarse-grained output of a fully three-dimensional model [14, 15]. Issues of stability were dealt with by using a training cost function that takes into account the predictions from several forward time steps and by excluding upper-tropospheric levels from the input features. This NN parameterization was reasonably accurate for short-term forecasts, but it led to climate drift on longer times scales and it could not be used for studies of climate. Thus, an ML parameterization has not yet been successfully learned from a three-dimensional high-resolution atmospheric model for use in studies of climate.

One approach that may help the robustness and stability of an ML parameterization is to ensure that it respect physical constraints such as energy conservation [18]. Using a random forest (RF) [19, 20] to train a parameterization has the advantage that the resulting parameterization automatically respects energy conservation (to the extent energy is linear in the predicted quantities) and non-negative surface precipitation [13]. These physical constraints are respected because the predictions of the RF are averages over subsets of the training dataset [19, 20]. The property that the RF predictions cannot go outside the convex hull of the training data may also

help ensure that an RF parameterization is robust when implemented in a global climate model (GCM). When an RF was used to emulate a conventional convective parameterization, it was found to lead to stable and accurate simulations of important climate statistics in tests with an idealized GCM [13].

Results

Learning a parameterization from high-resolution model output

In this study we train a new RF parameterization on coarse-grained output from a high-resolution three-dimensional model of a quasi-global atmosphere, and we show that the parameterization can be used at coarse resolution to reproduce the climate of the high-resolution simulation and to give insights into the dependence of parameterization performance on grid spacing. The model used is the System for Atmospheric Modeling (SAM) [21], and the domain is an equatorial beta plane of zonal width 6,912km and meridional extent 17,280km. The lower boundary condition is an ocean with a prescribed distribution of surface temperature (SST) that is zonally and hemispherically symmetric and reaches a maximum at the equator (the “qobs” SST distribution [22]). To reduce computational expense, we use hypohydrostatic rescaling (with a scaling factor of 4) which effectively increases the horizontal length scale of convection and allows us to use a coarser horizontal grid spacing of 12km than would be normally used in a cloud-system resolving simulation, while not affecting the large-scale dynamics [23, 24, 25, 26]. Further details of the model configuration are given in the Supplementary Information.

The high-resolution simulation (hi-res) exhibits organization on a wide range of length scales from the convective to the planetary scale (Fig. 1a). The largest-scale organization consists of two intertropical convergence zones (ITCZs) and an extratropical storm track in the midlatitudes of each hemisphere. The configuration used here in which the SST distribution is fixed and symmetric about the equator is a challenging test of our RF parameterization since the resulting circulation is known to be very sensitive to subgrid parameterizations, and coarse-resolution GCMs in this configuration give a range of tropical circulations from a strong single ITCZ to a double ITCZ [27]. We find there is a double ITCZ at high resolution for our model configuration, and this is likely dependent on the exact SST distribution used and the geometry of the domain. When the model is run with a horizontal grid spacing of 96km and thus eight times coarser horizontal resolution (x8), the double ITCZ switches to a much stronger single ITCZ (Fig. 1b) and the distribution of mean precipitation is strongly altered throughout the tropics (Fig. 2a). Extreme precipitation, which is important for impacts on society and ecosystems, is evaluated

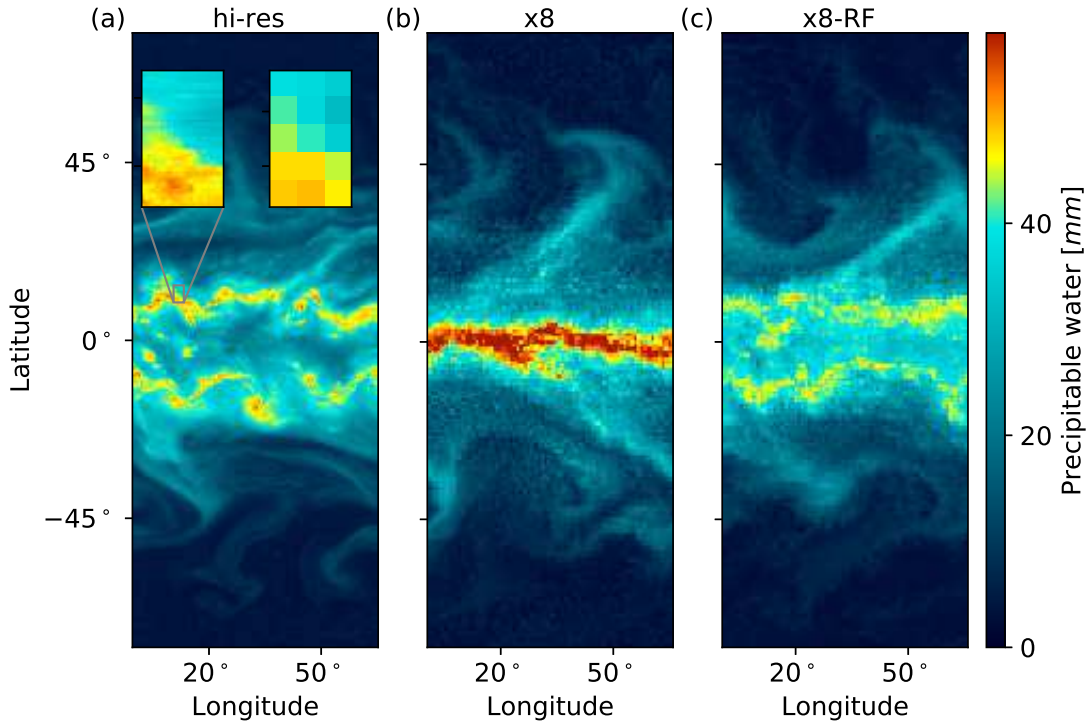


Figure 1: **Snapshots of column-integrated precipitable water taken from the statistical equilibrium of simulations.** (a) High-resolution simulation (hi-res), (b) coarse-resolution simulation (x8), and (c) coarse-resolution simulation with RF parameterization (x8-RF). Insets in (a) show (left) a zoomed-in region and (right) the same region but coarse-grained by a factor of 8 to the same grid spacing as in (b). The colorbar is saturated in parts of panel b.

here as the 99.9th percentile of 3-hourly precipitation; it is sensitive at all latitudes to changing from high to coarse resolution (Fig. 2b). In this study, we do not compare the results of the hi-res simulation to a coarse-resolution simulation with conventional convective and boundary-layer parameterization both because SAM is not equipped with such parameterizations and because the results in the tropics would be highly dependent on the specific choice of parameterizations for both mean precipitation [27] and extreme precipitation [4].

The RF parameterization predicts the effect of unresolved subgrid processes, including vertical advection and cloud and precipitation microphysics, on the resolved thermodynamic and moisture prognostic variables at each grid box and time step.

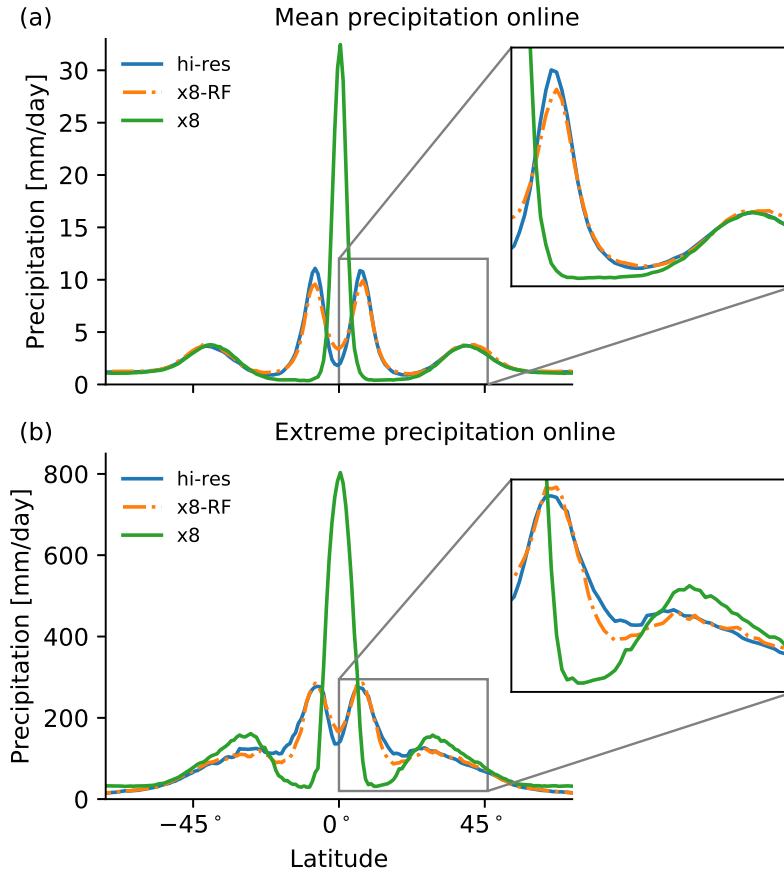


Figure 2: **Mean and extreme precipitation as a function of latitude.** (a) Zonal- and time-mean precipitation and (b) 99.9th percentile of 3-hourly precipitation, for the high-resolution simulation (hi-res; blue), and the coarse resolution simulation with the RF parameterization (x8-RF; orange dash-dotted) and without the RF parameterization (x8; green). For hi-res, the precipitation is coarse-grained to the grid-spacing of x8 prior to calculating the 99.9th percentile to give a fair comparison [28].

The turbulent diffusivity, radiative heating in the troposphere, and subgrid surface fluxes are also predicted. Subgrid momentum fluxes are not predicted, but this is not expected to strongly affect the results since we do not have topography that could generate strong gravity wave drag and since tropical convection occurs in regions of relatively weak shear in our simulations. The prognostic variables that are explicitly affected by the RF-parameterization are the liquid/ice water moist static energy (h_L), precipitating water mixing ratio (q_p), and total non-precipitating water mixing ratio (q_T). One RF is used for the combined tendencies due to vertical advection, cloud and precipitation microphysics and radiative heating. Subgrid tendencies for vertical advection and microphysics are calculated as the horizontal coarse-graining of the tendencies at high resolution minus the tendencies calculated from the model physics and dynamics using the coarse-grained prognostic variables as inputs. A second RF (with different features) is used to predict the turbulent diffusivity and the subgrid correction to the surface fluxes. The parameterization is local in time and in the horizontal, and we do not find it is necessary to include multiple time steps in the cost function to ensure stability unlike what was found in some previous studies with a different approach to calculating subgrid tendencies and a different machine learning algorithm [14, 15]. The Supplementary Information gives further details about the RFs and demonstrates that they respect energy conservation and non-negative surface precipitation (text S3).

Simulation with RF parameterization

A simulation with the RF parameterization at 96km grid spacing (x8-RF) was run using an initial condition taken from the statistical equilibrium of the x8 simulation with no RF parameterization. The x8-RF simulation transitions to a new statistical equilibrium with a double ITCZ similar to that in the high-resolution simulation (Fig. 1c) and it runs stably over long timescales (we have run it for a 1000 days). At statistical equilibrium, the distribution of mean precipitation closely resembles that of the high-resolution simulation (Fig. 2a), and the distribution of extreme precipitation is also remarkably well captured (Fig. 2b). Other measures such as eddy kinetic energy, mean zonal wind, mean meridional wind and mean q_T are also correctly captured by x8-RF (Table S2). Overall, these results show that using the RF subgrid parameterization brings the climate of the coarse-resolution simulation into close agreement with the climate of the high-resolution simulation.

The x8-RF simulation requires roughly 30 times less processor time than the high resolution simulation (for x16-RF the speed up is by roughly a factor of 120). Further increases in speed could be obtained by increasing the time step but this is

limited by the fall speed of precipitation. In the Supplementary Information (text S4), we present an alternative RF parameterization in which q_p is no longer treated as a prognostic variable; this alternative parameterization leads to a climate that is only slightly less accurate, and it could be used to achieve even faster simulations at coarse resolution.

Accuracy for different grid spacings

The fact that the RF parameterization is learned from a fully three-dimensional simulation with a wide range of length scales allows us to explore the longstanding question of whether there is a particular range of grid spacings for which a parameterization could be most successful. With increasing grid spacing, coarse-graining involves more averaging over different cloud elements which should make the subgrid tendencies more predictable, but the parameterization is then also responsible for more of the dynamics and physics.

To see which of these factors wins out, we train RF parameterizations for a range of coarse-graining factors from x4 to x32 and use them in simulations with corresponding grid spacings. We first describe the performance of the RFs on offline tests (i.e., when the RFs are not implemented in SAM) based on data withheld in training. The offline performance improves substantially as the grid spacing increases (Fig. 3a and compare Fig. 3c and 3e), consistent with the idea of more predictable subgrid tendencies with coarse graining over larger grid boxes. However, the accuracy of the resulting climate in the coarse-resolution simulations is worst for the largest grid spacing (Fig. 3b and compare Fig. 3d and 3f) presumably because more of the dynamics is subgrid and errors occur over larger grid boxes which outweighs the increase in predictability of the instantaneous subgrid tendencies. Offline performance is not indicative of online performance in this case. The degradation in online performance at large grid spacing is more pronounced for mean precipitation (Fig. 3b,d,f) as compared to extreme precipitation (Fig. S7). Fig. 3b also show the existence of a gray zone in our simulations over which a reduction in grid spacing from x8 to x4 does not improve the online performance of the parameterization even when a specific parameterization is trained for each grid spacing. Nevertheless, the performance at x4 is almost as good as at x8.

Discussion

The results presented here provide a step forward in demonstrating the viability of a parameterization of subgrid physics and dynamics learned from a high-resolution three dimensional simulation of the atmosphere. The results also give insights into

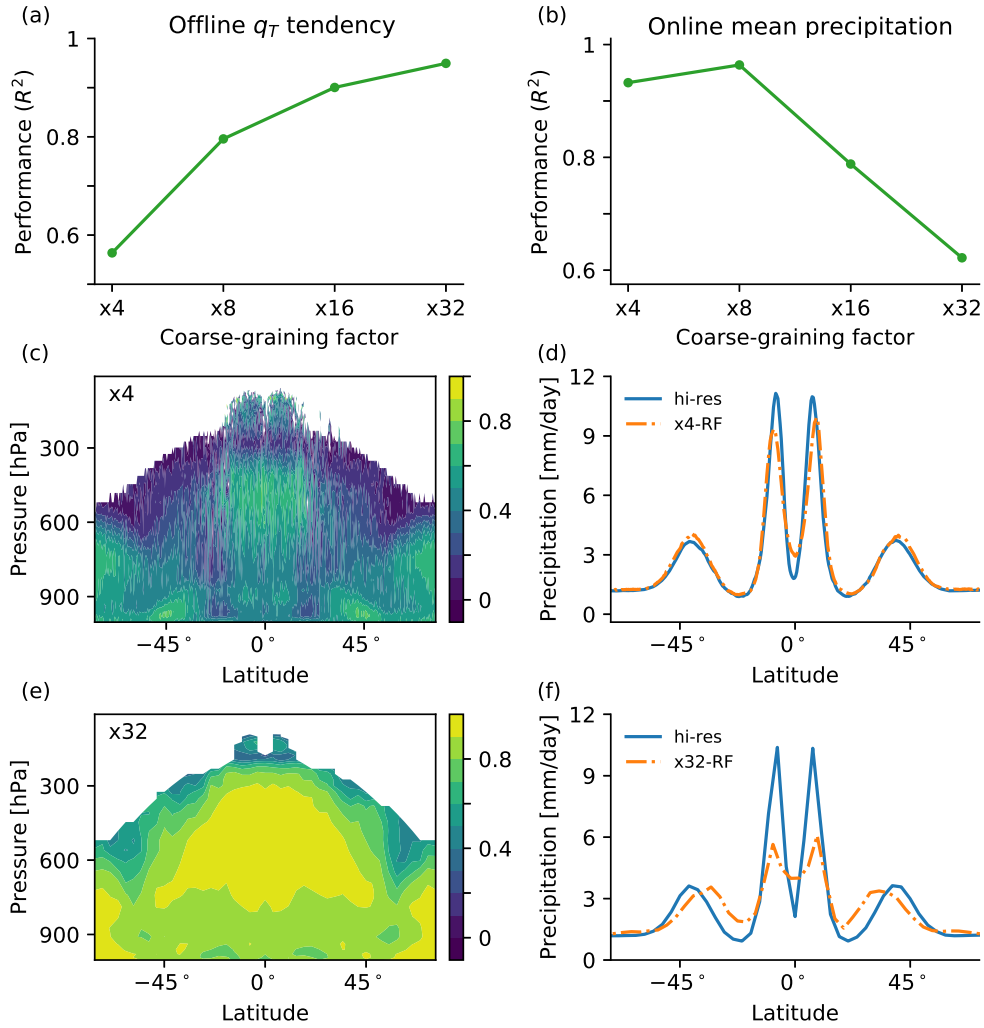


Figure 3: **Performance of the RF parameterization versus grid spacing.** (a) R^2 for the RF-predicted tendency of non-precipitating water (q_T), (b) R^2 for the mean precipitation versus latitude from the coarse simulations with an RF parameterization compared to hi-res, (c,e) R^2 for the RF-predicted tendency of q_T versus latitude and pressure for coarse graining by (c) x4 and (e) x32, and (d,f) mean precipitation versus latitude for (d) x4-RF (orange) and (f) x32-RF (orange) compared to hi-res (blue). In (a,c,e), R^2 is based on test data. In (c,e), R^2 is only shown where the variance is at least 0.1% of the mean variance over all latitudes and levels.

how well a parameterization can perform as a function of length scale, with implications not only for ML parameterizations but also for conventional parameterizations. Future research on ML parameterization must address questions such as how best to train over land regions with topography, but it should also continue to seek insights into the underlying physics and the nature of the parameterization problem.

Acknowledgements. We thank Bill Boos for providing the output from the high-resolution simulation, and we thank Daniel Koll and Nick Lutsko for helpful discussions. We acknowledge high-performance computing support from Cheyenne (doi:10.5065/D6RX99HX) provided by NCAR’s Computational and Information Systems Laboratory, sponsored by the National Science Foundation. We acknowledge support from the MIT Environmental Solutions Initiative, the EAPS Houghton-Lorenz postdoctoral fellowship, and NSF AGS-1552195.

- **Competing Interests.** The authors declares that they have no competing financial interests.
- Correspondence and requests for materials should be addressed to J.Y. (email: janniy@mit.edu).

References

- [1] Webb, M. J., Lambert, F. H. & Gregory, J. M. Origins of differences in climate sensitivity, forcing and feedback in climate models. *Clim. Dyn.* **40**, 677–707 (2013).
- [2] Sherwood, S. C., Bony, S. & Dufresne, J. Spread in model climate sensitivity traced to atmospheric convective mixing. *Nature* **505**, 37 (2014).
- [3] O’Gorman, P. A. Sensitivity of tropical precipitation extremes to climate change. *Nat. Geosci.* **5**, 697 (2012).
- [4] Wilcox, E. M. & Donner, L. J. The frequency of extreme rain events in satellite rain-rate estimates and an atmospheric general circulation model. *J. Climate* **20**, 53–69 (2007).
- [5] Ceppi, P. & Hartmann, D. L. Clouds and the atmospheric circulation response to warming. *J. Climate* **29**, 783–799 (2016).
- [6] Schneider, T. *et al.* Climate goals and computing the future of clouds. *Nat. Clim. Change* **7**, 3–5 (2017).

- [7] Bretherton, C. S. & Khairoutdinov, M. F. Convective self-aggregation feedbacks in near-global cloud-resolving simulations of an aquaplanet. *J. Adv. Model. Earth Sys.* **7**, 1765–1787 (2015).
- [8] Stevens, B. *et al.* DYAMOND: the DYnamics of the Atmospheric general circulation Modeled On Non-hydrostatic Domains. *Prog. Earth Plan. Sci.* **6**, 61 (2019).
- [9] Stouffer, R. J. Time scales of climate response. *J. Climate* **17**, 209–217 (2004).
- [10] Krasnopolsky, V. M., Fox-Rabinovitz, M. S. & Belochitski, A. A. Using ensemble of neural networks to learn stochastic convection parameterizations for climate and numerical weather prediction models from data simulated by a cloud resolving model. *Adv. Artif. Neural Syst.* **2013**, 5 (2013).
- [11] Gentine, P., Pritchard, M., Rasp, S., Reinaudi, G. & Yacalis, G. Could machine learning break the convection parameterization deadlock? *Geophys. Res. Lett.* **45**, 5742–5751 (2018).
- [12] Rasp, S., Pritchard, M. S. & Gentine, P. Deep learning to represent subgrid processes in climate models. *Proc. Natl. Acad. Sci. U.S.A.* **115**, 9684–9689 (2018).
- [13] O’Gorman, P. A. & Dwyer, J. G. Using machine learning to parameterize moist convection: Potential for modeling of climate, climate change, and extreme events. *J. Adv. Model. Earth Sys.* **10**, 2548–2563 (2018).
- [14] Brenowitz, N. D. & Bretherton, C. S. Prognostic validation of a neural network unified physics parameterization. *Geophys. Res. Lett.* **45**, 6289–6298 (2018).
- [15] Brenowitz, N. D. & Bretherton, C. S. Spatially extended tests of a neural network parametrization trained by coarse-graining. *J. Adv. Model. Earth Sys.* **11**, 2727–2744 (2019).
- [16] Bolton, T. & Zanna, L. Applications of deep learning to ocean data inference and subgrid parameterization. *J. Adv. Model. Earth Sys.* **11**, 376–399 (2019).
- [17] Rasp, S. Online learning as a way to tackle instabilities and biases in neural network parameterizations. *arXiv preprint arXiv:1907.01351* (2019).
- [18] Beucler, T., Rasp, S., Pritchard, M. & Gentine, P. Achieving conservation of energy in neural network emulators for climate modeling. *arXiv preprint arXiv:1906.06622* (2019).

- [19] Breiman, L. Random forests. *Machine learning* **45**, 5–32 (2001).
- [20] Hastie, T., Tibshirani, R. & Friedman, J. *The elements of statistical learning* (Springer, 2001), 2nd edn.
- [21] Khairoutdinov, M. F. & Randall, D. A. Cloud resolving modeling of the ARM summer 1997 IOP: Model formulation, results, uncertainties, and sensitivities. *J. Atmos. Sci.* **60**, 607–625 (2003).
- [22] Neale, R. B. & Hoskins, B. J. A standard test for AGCMs including their physical parametrizations: I: The proposal. *Atmos. Sci. Lett.*, **1**, 101–107 (2000).
- [23] Kuang, Z., Blossey, P. N. & Bretherton, C. S. A new approach for 3D cloud-resolving simulations of large-scale atmospheric circulation. *Geophys. Res. Lett.* **32** (2005).
- [24] Garner, S. T., Frierson, D. M. W., Held, I. M., Pauluis, O. & Vallis, G. K. Resolving convection in a global hypohydrostatic model. *J. Atmos. Sci.* **64**, 2061–2075 (2007).
- [25] Boos, W. R., Fedorov, A. & Muir, L. Convective self-aggregation and tropical cyclogenesis under the hypohydrostatic rescaling. *J. Atmos. Sci.* **73**, 525–544 (2016).
- [26] Fedorov, A. V., Muir, L., Boos, W. R. & Studholme, J. Tropical cyclogenesis in warm climates simulated by a cloud-system resolving model. *Clim. Dyn.* **52**, 107–127 (2019).
- [27] Möbis, B. & Stevens, B. Factors controlling the position of the intertropical convergence zone on an aquaplanet. *J. Adv. Model. Earth Sys.* **4**, M00A04 (2012).
- [28] Chen, C. T. & Knutson, T. On the verification and comparison of extreme rainfall indices from climate models. *J. Climate* **21**, 1605–1621 (2008).

Supplementary Information for “Use of machine learning to improve simulations of climate”

Janni Yuval¹ and Paul A. O’Gorman¹

¹Massachusetts Institute of Technology, Cambridge, Massachusetts 02139, USA

S1 Methods

S1.1 Model

The model used in this study is the System for Atmospheric Modeling (SAM), version 6.3 [1], which is a relatively efficient model that integrates the anelastic equations of motion in Cartesian coordinates. The bulk microphysics scheme is single moment with precipitating water consisting of rain, snow and graupel, and non-precipitating water consisting of water vapor, cloud water and cloud ice. Cloud ice experience sedimentation, and we include the surface sedimentation flux (which is small) in all reported surface precipitation statistics. The subgrid-scale turbulent closure is a Smagorinsky-type scheme. The radiation scheme is based on parameterizations from the National Center for Atmospheric Research (NCAR) Community Climate Model (CCM) version 3.5 [2].

The equations for the prognostic thermodynamic and moisture variables in SAM are important for our study and may be written as [1]

$$\frac{\partial h_L}{\partial t} = -\frac{1}{\rho_0} \frac{\partial}{\partial x_i} (\rho_0 u_i h_L + F_{h_L i}) - \frac{1}{\rho_0} \frac{\partial}{\partial z} (L_p P_{\text{tot}} + L_n S) + \left(\frac{\partial h_L}{\partial t} \right)_{\text{rad}}, \quad (\text{S1})$$

$$\frac{\partial q_T}{\partial t} = -\frac{1}{\rho_0} \frac{\partial}{\partial x_i} (\rho_0 u_i q_T + F_{q_T i}) + \frac{1}{\rho_0} \frac{\partial}{\partial z} (S) - \left(\frac{\partial q_T}{\partial t} \right)_{\text{mic}}, \quad (\text{S2})$$

$$\frac{\partial q_p}{\partial t} = -\frac{1}{\rho_0} \frac{\partial}{\partial x_i} (\rho_0 u_i q_p + F_{q_p i}) + \frac{1}{\rho_0} \frac{\partial}{\partial z} (P_{\text{tot}}) + \left(\frac{\partial q_p}{\partial t} \right)_{\text{mic}}, \quad (\text{S3})$$

where $h_L = c_p T + gz - L_c(q_c + q_r) - L_s(q_i + q_s + q_g)$ is the liquid/ice water static energy; ρ_0 is the horizontal-mean air density; q_T is the non-precipitating water mixing ratio which is the sum of the mixing ratios of water vapor (q_v), cloud water (q_c) and cloud ice (q_i); q_p is the total precipitating water mixing ratio which is the sum of the mixing ratios of rain (q_r), snow (q_s) and graupel (q_g); F_{A_i} is the diffusive flux of variable A ; $u_i = (u, v, w)$ is the three-dimensional wind; P_{tot} is the total precipitation mass flux (defined positive downwards); S is the total sedimentation mass flux (defined positive downwards); the subscript “rad” denotes the tendency due to radiative heating; the subscript “mic” represents the microphysical tendency due to autoconversion, aggregation,

collection, and evaporation and sublimation of precipitation; L_c , L_f and L_s are the latent heat of condensation, fusion and sublimation, respectively; $L_p = L_c + L_f(1 - \omega_p)$ is the effective latent heat associated with precipitation and ω_p is the partition function for precipitation; $L_n = L_c + L_f(1 - \omega_n)$ is the effective latent heat associated with non-precipitating condensate and ω_n is the partition function for non-precipitating condensate.

S1.2 Simulations

All simulations are run on the same quasi-global domain with an equivalent latitude range from -78.5° to 78.5° and longitudinal extent of 62.2° at the equator. There are 48 vertical levels with spacing that increases from 85m at the surface to 1650m in the stratosphere. The default time step is 24 seconds, and this is automatically halved whenever the CFL condition would be otherwise violated. The insolation is set at perpetual equinox without a diurnal cycle. The simulations are run with a zonally symmetric “qobs” [3] sea surface temperature (SST) distribution which varies between 300.15K at the equator and 273.15K at the poleward boundaries. Surface albedo is a function of latitude, and there is no sea ice in the model. Hypohydrostatic rescaling of the vertical momentum equation with a rescaling factor of 4 increases the horizontal length scale of convection while leaving the large-scale dynamics unaffected and still retaining a very large range of length scales in the hi-res simulation [4, 5, 6, 7, 8]. A similar configuration of SAM with hypohydrostatic rescaling (though not at equinox) was recently used to investigate tropical cyclogenesis in warm climates [8]. Furthermore, SAM was also used in previous studies that developed ML parameterizations [9, 10].

The hi-res simulation has 12km grid spacing (recalling that hypohydrostatic rescaling is used) and was spun up for 100 days. It was then run for 500 days with three-dimensional snapshots of the prognostic variables, radiative heating and turbulent diffusivity saved every three hours. Results for the hi-res simulation are averaged over 500 days. Coarse-resolution simulations were run for 600 days, with the first 100 days of each simulation treated as spinup, and results averaged over the last 500 days. Simulations with the RF parameterization start with initial conditions taken from simulations without the RF parameterization (at the same resolution).

The version of SAM that was used for the hi-res simulation had some minor discretization errors, the most important of which was in the Coriolis parameter in the meridional momentum equation. Effectively the Coriolis parameter is shifted by a distance of half a gridbox (6km) to the south. To avoid wasteful rerunning of the expensive hi-res simulation, we instead shifted the Coriolis parameter in the meridional momentum equation by 6km (half of the hi-res gridbox size) in all coarse-resolution simulations for consistency with the hi-res simulation.

S1.3 Coarse graining the high-resolution simulation

For each 3-hourly snapshot from the hi-res simulation, we coarse-grain the prognostic variables (u, v, w, h_L, q_T, q_p), the tendencies of h_L, q_T , and q_p (eqs. S1-S3), the surface fluxes and the turbulent diffusivity. This coarse-graining and the subsequent calculation of subgrid contributions is performed in post-processing.

Coarse-graining is performed by horizontal averaging onto a coarser grid as follows:

$$\overline{A}(i, j, k) = \frac{1}{N^2} \sum_{l=N(i-1)+1}^{l=Ni} \sum_{m=N(l-1)+1}^{m=Nl} A(l, m, k), \quad (\text{S4})$$

where A is the high-resolution variable, \overline{A} is the coarse-grained variable, N is the coarse graining factor, k is the index of the vertical level, and i, j (l, m) are the discrete indices of the longitudinal and latitudinal coordinates at coarse resolution (high resolution).

Different coarse-graining factors were used to study how well the ML-parameterization performs at different resolutions. The horizontal grid spacings that were used were 48km (x4), 96km (x8), 192km (x16), and 384km (x32). The hi-res simulation has a grid size of 576x1440, and coarse graining it by factors of 4, 8 and 16 results in grid sizes of 144x360, 72x180 and 36x90, respectively. These grids can be simulated in SAM. Unfortunately, coarse-graining the hi-res simulation by a factor of 32 results in a grid (18x45) which cannot run on SAM. Instead, the number of grid points in the latitudinal direction in these simulations was increased to 48 points (18x48 grid size), leading to a slightly larger domain, and the presented results were interpolated to the coarse-grained high-resolution grid (with 45 points in the latitudinal direction).

We define the resolved tendency as the tendency calculated using the dynamics and physics of model with the coarse-grained prognostic variables as inputs. The tendencies due to unresolved (subgrid) physical processes were calculated as the difference between the coarse-grained tendency and the resolved tendency. The subgrid tendency for a given process is then written as

$$\left(\frac{\partial \overline{B}}{\partial t}\right)^{\text{subgrid}} = \frac{\partial \overline{B}}{\partial t}(h_L, q_T, q_p, u, v, w) - \frac{\partial B}{\partial t}(\overline{h}_L, \overline{q}_T, \overline{q}_p, \overline{u}, \overline{v}, \overline{w}) \quad (\text{S5})$$

where B is a certain variable, $\frac{\partial \overline{B}}{\partial t}(h_L, q_T, q_p, u, v, w)$ is the coarse-grained high-resolution tendency of that variable due to the process, $\frac{\partial B}{\partial t}(\overline{h}_L, \overline{q}_T, \overline{q}_p, \overline{u}, \overline{v}, \overline{w})$ is the resolved tendency due to the process, and $\left(\frac{\partial \overline{B}}{\partial t}\right)^{\text{subgrid}}$ is the subgrid tendency due to the process. For example, the subgrid tendency of h_L due to vertical advection is

$$\left(\frac{\partial \overline{h}_L}{\partial t}\right)_{\text{vert. adv.}}^{\text{subgrid}} = - \left(w \frac{\partial \overline{h}_L}{\partial z} - \overline{w} \frac{\partial \overline{h}_L}{\partial z} \right). \quad (\text{S6})$$

Subgrid and resolved contributions are defined in a similar way for the surface fluxes of h_L and q_T .

S1.4 Choice of outputs for the RF parameterization

The RF parameterization predicts the combined tendencies for the following processes: subgrid vertical advection of h_L , q_T , and q_p , subgrid cloud and precipitation microphysical tendencies included in $\left(\frac{\partial q_p}{\partial t}\right)_{\text{mic}}$, subgrid falling of precipitation and subgrid sedimentation of cloud ice, and the total radiative heating tendency (see below). The RF parameterization also predicts subgrid corrections to the surface fluxes of h_L and q_T .

For radiation, the RF parameterization predicts the total radiative heating and not the subgrid part. The choice to predict the radiative heating tendency rather than predicting its subgrid correction was mainly motivated by the complexity of calculating subgrid radiative heating tendencies

in post-processing. Radiative heating is not predicted above 11.8km since the RF has poor performance above this level in offline tests. Instead the SAM prediction for radiative heating is used at those levels. Including the RF prediction for radiative heating at all stratospheric levels leads to a temperature drift in the stratosphere when RF-tend is implemented in SAM (though tropospheric fields are still similar to the presented results). We checked that the results were not sensitive to the exact choice of cutoff level.

For turbulent diffusion, we chose to predict the coarse-grained turbulent diffusivity rather than the tendencies due to turbulent diffusion. This approach has the advantages that it constrains the diffusive fluxes to be down-gradient and that the same diffusivity is applied to all thermodynamic and moisture variables (unlike if we predicted the effective diffusivity based on coarse-grained fluxes and gradients for each variable separately). In order to reduce computation time, the diffusivity is not predicted above 5.7km where it is relatively small, and the diffusivity calculated in SAM is used instead. We checked that the results were not sensitive to the exact choice of cutoff level. We did not apply the RF predicted diffusivity to the horizontal diffusivity or to any of the momentum variables.

The RF parameterization does not predict tendencies due to subgrid momentum fluxes or due to horizontal fluxes, and these could be studied in future work. The need to include subgrid momentum fluxes would likely be greater if topography was included (due to gravity wave drag) and could in principle be greater with other distributions of insolation (due to convection occurring to a greater extent in regions of strong shear), but these considerations are beyond the scope of this study.

S1.5 Structure of the RF parameterization

The RF parameterization consists of two RFs. We assume that the subgrid contributions depend only on the vertical column of the grid point at the current time step, and therefore the RFs are local in time and local in the horizontal.

The first RF, referred to as RF-tend, predicts the combined tendencies for all processes except for turbulent diffusion. The features (inputs) for RF-tend ($X_{\text{RF-tend}}$) are chosen to be the vertical profiles (discretized on model levels) of the resolved temperature (T), q_T , q_p , and the distance from the equator ($|y|$). Hence $X_{\text{RF-tend}} = (T, q_T, q_p, |y|)$, giving $48 \times 3 + 1 = 145$ features. The distance from the equator serves as a proxy for the SST, surface albedo and solar insolation, as these are only a function of this distance in the simulations. The outputs of RF-tend ($Y_{\text{RF-tend}}$) are vertical profiles of combined tendencies of h_L , q_T and q_p due to subgrid vertical advection, subgrid microphysics, subgrid sedimentation and falling of precipitation, and total radiative heating. Hence $Y_{\text{RF-tend}} = (h_L^{\text{subg-tend}}, q_T^{\text{subg-tend}}, q_p^{\text{subg-tend}})$, giving $48 \times 3 = 144$ outputs.

A second RF, referred to as RF-diff, predicts the turbulent diffusivity and the subgrid corrections for the surface fluxes. As discussed in the previous section, the predicted turbulent diffusivity is only applied in the lower troposphere ($z \leq 5.7\text{km}$). The features of RF-diff are chosen to be the lower tropospheric vertical profiles of T , q_T , zonal wind (u), meridional wind (v), surface wind speed ($\text{wind}_{\text{surf}}$), and distance from the equator, so that $X_{\text{RF-diff}} = (T, q_T, u, v, \text{wind}_{\text{surf}}, |y|)$, giving $4 \times 15 + 1 + 1 = 62$ features, since there are 15 levels below 5.7km. The outputs of RF-diff are the subgrid corrections for the surface fluxes of h_L and q_T , and the lower tropospheric vertical profile of the turbulent diffusivity, so that $Y_{\text{RF-diff}} = (h_L^{\text{surf-flux}}, q_T^{\text{surf-flux}}, \text{diffusivity})$, giving $1 + 1 + 15 = 17$ outputs. Since the meridional velocity is statistically anti-symmetric with respect to reflection around the equator, the meridional wind in the southern hemisphere is multiplied by -1 when it is

taken as a feature for the RF to help ensure that the RF is not learning non-physical relationships between inputs and outputs that could artificially improve our results. We include the wind variables as features for RF-diff because they improve the prediction of the diffusivity and subgrid surface fluxes. Adding wind features to RF-tend does not improve the accuracy of the predicted tendencies.

Surface precipitation is not predicted separately by the RF parameterization but is rather diagnosed (including any surface sedimentation) as the sum of the resolved precipitation and the subgrid correction ($P_{\text{tot}}^{\text{subgrid}}(z=0) + S^{\text{subgrid}}(z=0)$) which is calculated from water conservation as

$$P_{\text{tot}}^{\text{subgrid}}(z=0) + S^{\text{subgrid}}(z=0) = - \int_0^\infty \left(q_p^{\text{subg-tend}} + q_T^{\text{subg-tend}} \right) \rho_0 dz. \quad (\text{S7})$$

S1.6 Training, testing and choice of hyperparameters

Before training the RFs, each output variable is standardized by removing the mean and rescaling to unit variance. For output variables with multiple vertical levels, the mean and variance are calculated across all levels used for that output variable.

We use 337.5 days of 3-hourly model output from the hi-res simulation to calculate the features and outputs of the RFs. This model output was divided into a training dataset, validation dataset and a test dataset. The training dataset was obtained from the first 270 days (80% of the data) of the hi-res simulation, the validation data set was obtained from the following 33.75 days (10% of the data), and the test data was obtained from the last 33.75 days (10% of the data). (After tuning the hyperparameters, we expanded the training dataset to include the validation dataset for use in the final training process of the RFs used in SAM.) In order to reduce the correlation between different samples in our datasets, at each time step that was used, we randomly subsample atmospheric columns at each latitude. For coarse-graining factors of x4, x8 and x16, we randomly select 10, 20 and 25 longitudes, respectively, at each latitude for every time step. For x32, the amount of coarse-grained output is relatively limited and so we do not subsample. This results in test and validation dataset sizes of 972, 360 samples for x4 and x8, 607, 770 samples for x16 and 218, 790 samples for x32. The amount of training data used is one of the hyperparameters we tuned as described below.

To train the RFs, we use the RandomForestRegressor class from scikit-learn package [11] version 0.21.2. During the training process, different hyperparameters may be tuned to improve the performance of the RFs. The most important hyperparameters that we tuned are the number of trees in each forest, the minimum number of samples at each leaf node, and the number of training samples. Fig. S1 shows the coefficient of determination (R^2) evaluated on the validation dataset for different combinations of hyperparameters. We stress that unlike standard supervised machine learning tasks, higher accuracy on test data is not our only goal. We also want to have a fast RF since it will be called many times when used in a simulation, and we do not want to have an RF that is overly large in memory since it will need to be stored on each core (or possibly shared across all cores in a node). Based on a compromise between RF accuracy, memory demands and speed when the RF is implemented in SAM, for coarse-graining factors of x4, x8 and x16 we chose 10 trees in each RF, a minimum of 20 samples in each leaf and 5,000,000 training samples. However, fewer training samples were available for x32, and in order to have a similar size of RFs in this case, a minimum of 7 samples in each leaf were taken. For x8, RF-tend is 0.78GB and RF-diff is 0.20GB when stored in netcdf format at single precision. We found that this size in memory did not pose a problem when running across multiple cores, but in the event that memory did pose a problem, we

emphasize that the RF parameterization can achieve very similar accuracy at a smaller size. For example, we reduced the number of trees in RF-tend from 10 to 5 which reduces its size in memory by more than a factor of two to 0.35GB without any noticeable difference in the results when it is implemented in SAM at coarse resolution.

S2 Offline performances on the test dataset

Offline performance is evaluated using the coefficient of determination (R^2) as applied to the unscaled output variables. R^2 is plotted for outputs of the RF parameterization as a function of the latitude and pressure in Fig. S2. R^2 is generally higher in the lower and middle troposphere, though performance does vary across outputs. Generally, the RFs tend to underestimate the variance in predictions compared to the true variance, although less so for larger coarse-graining factors (Fig. S3).

R^2 for the different outputs (combining data from all vertical levels for a given output) at different coarse-graining factors are given in Table S1. It is helpful to think of the variables the RFs predict as having two components – a predictable component and a stochastic component. For smaller grid spacing, the stochastic component is larger, and therefore the prediction task becomes more difficult (Table S1). Therefore, the relatively low R^2 at higher resolution does not necessarily imply that the RF does not predict the predictable component accurately.

RF-tend is also able to accurately predict the instantaneous surface precipitation rate (Fig. S4) with $R^2 = 0.99$ based on the test dataset for x8. The predicted precipitation (including any surface sedimentation) is the sum of the resolved precipitation and the predicted subgrid correction ($P_{\text{tot}}^{\text{subgrid}}(z = 0) + S^{\text{subgrid}}(z = 0)$) which is calculated from equation S7.

S3 Non-negative surface precipitation and conservation of energy

The RF parameterization does a good job in respecting physical constraints because the constraints are respected by the training data and the RF predictions are averages over subsets of the training data [12]. In particular, the RF parameterization never predicts non-negative surface precipitation (Fig.S4). Similarly, in the remainder of this section we show that the RF parameterization conserves energy in the absence of external forcing (i.e., in the absence of radiative heating and surface fluxes of h_L).

RF-diff automatically respects energy conservation in the absence of external forcing since it predicts the turbulent diffusivity rather than the diffusive tendencies. To check energy conservation for RF-tend, we integrate the evolution equation for h_L (eq. S1) in the vertical with density weighting, and then consider the contributions to the resulting equation that come from RF-tend (denoted with a superscript subgrid) to give an energy-conservation residual:

$$\text{residual} = \int_0^\infty \rho_0 \left(\frac{\partial h_L}{\partial t} \right)_{\text{no-rad}}^{\text{subgrid}} dz + \bar{L}_p P_{\text{tot}}^{\text{subgrid}}(z=0) + \bar{L}_n S^{\text{subgrid}}(z=0). \quad (\text{S8})$$

Here $\left(\frac{\partial h_L}{\partial t} \right)_{\text{no-rad}}^{\text{subgrid}}$ is the subgrid tendency of h_L but excluding the contribution from radiative heating which is an external forcing. This tendency was evaluated by training a new RF-tend that predicts the radiative heating tendency and the sum of other tendencies of h_L as separate outputs. This RF-tend performed similarly to our default RF-tend in all other regards. In deriving equation S8, we have neglected subgrid correlations between L_p and P_{tot} and between L_n and S , and as a result the residual will not be exactly zero even for the true subgrid tendencies. In addition, in evaluating the residual, the column energy change due to subgrid surface precipitation and sedimentation ($\bar{L}_p P_{\text{tot}}^{\text{subgrid}}(z=0) + \bar{L}_n S^{\text{subgrid}}(z=0)$) was approximated to be $\bar{L}_p (P_{\text{tot}}^{\text{subgrid}}(z=0) + S^{\text{subgrid}}(z=0))$ so that we could evaluate it using equation S7. This approximation leads to a small error to the extent that there is surface sedimentation.

The distribution of the energy-conservation residual for the true subgrid tendencies is shown in Fig. S5a and for the RF-predicted subgrid tendencies in Fig. S5b. In general, the residuals are very small, and the distribution of the residuals is similar for the true subgrid tendencies and the RF-predicted subgrid tendencies. The difference between the true and the RF-predicted residuals for each column was also calculated, and its distribution is shown in Fig. S5c.

Fig. S5b demonstrates that the RF parameterization respects energy conservation to a high degree of accuracy (less than 2% of the data has residuals that are larger in amplitude than 1W m^{-2}). The root-mean-square error in energy conservation is 0.35W m^{-2} and the mean bias error is 0.11W m^{-2} . We note that a similar mean bias error is found in the calculation of the energy-conservation residual from the true subgrid tendencies, and both are likely a result of the approximations we used in the calculation of the energy conservation residual rather than a violation of energy conservation (the mean bias error found in Fig. S5c is 0.0001W m^{-2}). The root-mean-square error of 0.35W m^{-2} is substantially smaller than a reported value of 92W m^{-2} in a previous study that used a NN to learn from a quasi-global simulation [9] with the caveat that the metric of errors in energy conservation in that study also included errors in predicted radiative heating and surface fluxes. We note also that energy conservation for a NN parameterization can be enforced by including it as a constraint in the NN architecture [13].

S4 RF parameterization without using precipitating water as a variable

Here we describe an alternative RF parameterization approach in which q_p is not used as a variable. This alternative RF parameterization leads to stable simulations when implemented in SAM, and it gives similarly accurate results to the default approach for mean precipitation, but less accurate results for extreme precipitation in midlatitudes (Fig. S6). Since the alternative RF parameterization does not take q_p as an input, SAM in this case does not include q_p as a prognostic variable. Such a parameterization could be potentially very useful since q_p is a fast variable that limits the size of the timestep at coarse resolution.

The equations for the prognostic water and energy variables in SAM are described in eqs. S1-S3. We define a new prognostic energy variable (H_L) that does not include the precipitating water (q_p):

$$H_L = c_p T + gz - L_c q_c - L_s q_i. \quad (\text{S9})$$

This can be written in terms of the original energy variable h_L as

$$H_L = h_L + L_p q_p \quad (\text{S10})$$

where, $L_p = L_c + L_f(1 - \omega_p)$ and ω_p is the partition function for precipitation which depends only on temperature in SAM [1]. In the following, we account for vertical variations of L_p in the vertical but neglect the smaller variations in the horizontal and in time. Taking the derivative with respect to time of equation S10 gives

$$\frac{\partial H_L}{\partial t} = \frac{\partial h_L}{\partial t} + L_p \frac{\partial q_p}{\partial t}. \quad (\text{S11})$$

Substituting equations S1 and S3 into equation S11, we get a prognostic equation for H_L :

$$\begin{aligned} \frac{\partial H_L}{\partial t} = & -\frac{1}{\rho_0} \frac{\partial}{\partial x_i} (\rho_0 u_i H_L) - \frac{1}{\rho_0} \frac{\partial}{\partial z} (L_n S) + L_p \left(\frac{\partial q_p}{\partial t} \right)_{\text{mic}} + \left(\frac{\partial h_L}{\partial t} \right)_{\text{rad}} \\ & - \frac{1}{\rho_0} \frac{\partial F_{H_L i}}{\partial x_i} + \frac{1}{\rho_0} \frac{\partial L_p}{\partial z} (\rho_0 w q_p + F_{q_p z} - P_{\text{tot}}) \end{aligned} \quad (\text{S12})$$

where $F_{H_L i} = F_{h_L i} + L_p F_{q_p i}$ and the last term on the right hand side results from heating from phase changes of precipitation.

Our aim is to make a parameterization for coarse-resolution simulations that does not include q_p . Therefore we assume that at coarse resolution we can neglect the horizontal fluxes of q_p and the time derivative of q_p in equation S3. Integrating equation S3 vertically over the column and neglecting surface diffusive fluxes of q_p then gives an expression for the surface precipitation rate:

$$P_{\text{tot}}(z=0) = - \int_0^\infty \left(\frac{\partial q_p}{\partial t} \right)_{\text{mic}} dz. \quad (\text{S13})$$

The RF parameterization without q_p is similar in most respects to the RF parameterization with q_p , but some changes are needed. First, RF-tend does not use q_p as a feature or predict its tendency as an output, and it predicts the tendency of H_L rather than the tendency of h_L . Thus, the features for RF-tend are $X = (T, q_T, |y|)$, and the outputs are $y = (H_L^{\text{subg-tend}}, q_T^{\text{subg-tend}})$. RF-diff is changed to predict the subgrid surface flux of H_L instead of h_L . Second, RF-tend in this version

predicts for $H_L^{\text{subg-tend}}$ the subgrid vertical advection and subgrid sedimentation terms added to the total value of $L_p \left(\frac{\partial q_p}{\partial t} \right)_{\text{mic}} + \left(\frac{\partial h_L}{\partial t} \right)_{\text{rad}} + \frac{1}{\rho_0} \frac{\partial L_p}{\partial z} (\rho_0 w q_p + F_{q_p z} - P_{\text{tot}})$ in equation S12. Third, we do not apply the RF tendency of q_T due to subgrid vertical advection and sedimentation above 11.8km to avoid a feedback that lead to a severe change in the global circulation. (This is likely to be a similar issue to an instability that occurred in a previous study on ML parameterization that also did not use q_p as a prognostic variable and in which this instability was dealt with by not including certain upper-level variables as features [10].) To avoid over-fitting the results presented here, we chose the same upper-level cutoff for these q_T tendencies (11.8km) as was also used for radiative heating. We tested different upper-level cutoffs (11km, 9.5km) and different combinations of cutoff levels (different cutoff levels for each process) and found that all these choices led to simulations with qualitatively similar results.

When implementing the alternative RF parameterization in SAM, we remove q_p as a prognostic variable and change from h_L to H_L as a prognostic variable. We diagnose surface precipitation using equation S13 (plus any surface sedimentation). The approximations used in deriving equation S13 can result in negative instantaneous surface precipitation in rare cases. However, the surface precipitation averaged over 3 hours in the SAM simulations with this RF parameterization is negative less than 1% of the time and the negative values are smaller in magnitude than 0.2mm day^{-1} .

References

- [1] Khairoutdinov, M. F. & Randall, D. A. Cloud resolving modeling of the ARM summer 1997 IOP: Model formulation, results, uncertainties, and sensitivities. *J. Atmos. Sci.* **60**, 607–625 (2003).
- [2] Kiehl, J. T. *et al.* The National Center for Atmospheric Research community climate model: CCM3. *J. Climate* **11**, 1131–1149 (1998).
- [3] Neale, R. B. & Hoskins, B. J. A standard test for AGCMs including their physical parametrizations: I: The proposal. *Atmos. Sci. Lett.*, **1**, 101–107 (2000).
- [4] Kuang, Z., Blossey, P. N. & Bretherton, C. S. A new approach for 3D cloud-resolving simulations of large-scale atmospheric circulation. *Geophys. Res. Lett.* **32** (2005).
- [5] Garner, S. T., Frierson, D. M. W., Held, I. M., Pauluis, O. & Vallis, G. K. Resolving convection in a global hypohydrostatic model. *J. Atmos. Sci.* **64**, 2061–2075 (2007).
- [6] Ma, D., Boos, W. & Kuang, Z. Effects of orography and surface heat fluxes on the south asian summer monsoon. *J. Climate* **27**, 6647–6659 (2014).
- [7] Boos, W. R., Fedorov, A. & Muir, L. Convective self-aggregation and tropical cyclogenesis under the hypohydrostatic rescaling. *J. Atmos. Sci.* **73**, 525–544 (2016).
- [8] Fedorov, A. V., Muir, L., Boos, W. R. & Studholme, J. Tropical cyclogenesis in warm climates simulated by a cloud-system resolving model. *Clim. Dyn.* **52**, 107–127 (2019).
- [9] Brenowitz, N. D. & Bretherton, C. S. Prognostic validation of a neural network unified physics parameterization. *Geophys. Res. Lett.* **45**, 6289–6298 (2018).
- [10] Brenowitz, N. D. & Bretherton, C. S. Spatially extended tests of a neural network parametrization trained by coarse-graining. *J. Adv. Model. Earth Sys.* **11**, 2727–2744 (2019).
- [11] Pedregosa, F. *et al.* Scikit-learn: Machine learning in python. *J. Mach. Learn. Res.* **12**, 2825–2830 (2011).
- [12] O’Gorman, P. A. & Dwyer, J. G. Using machine learning to parameterize moist convection: Potential for modeling of climate, climate change, and extreme events. *J. Adv. Model. Earth Sys.* **10**, 2548–2563 (2018).
- [13] Beucler, T., Rasp, S., Pritchard, M. & Gentine, P. Achieving conservation of energy in neural network emulators for climate modeling. *arXiv preprint arXiv:1906.06622* (2019).
- [14] Chen, C.-T. & Knutson, T. On the verification and comparison of extreme rainfall indices from climate models. *J. Climate* **21**, 1605–1621 (2008).

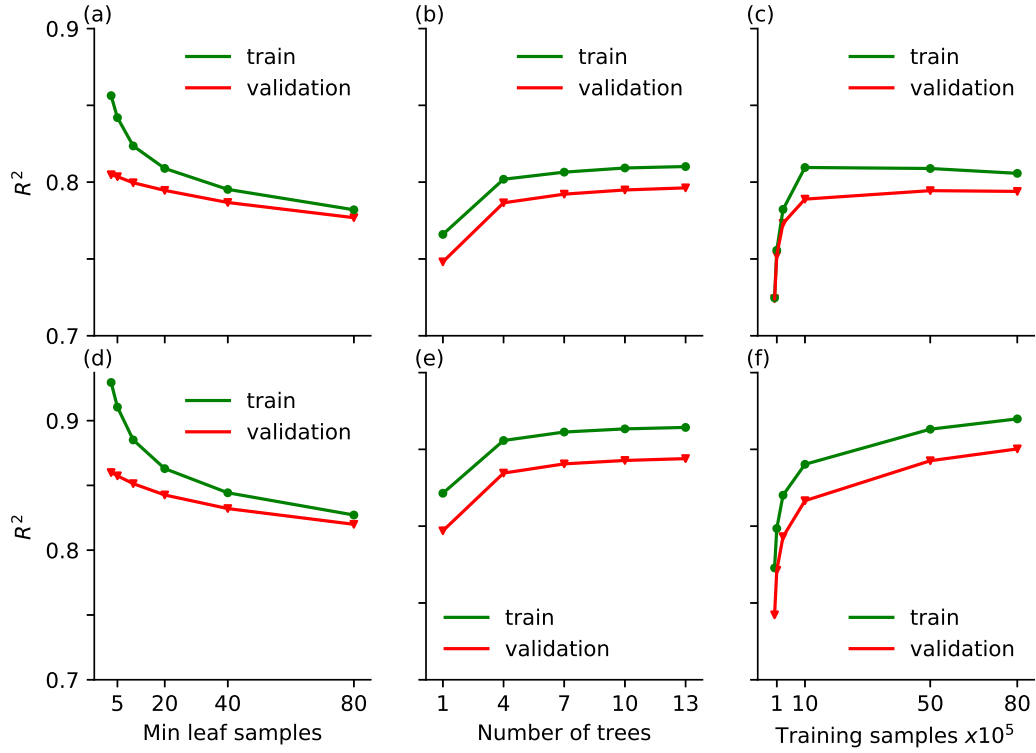


Figure S1: Coefficient of determination (R^2) for RF-tend (panels a-c, R^2 calculated for $q_T^{\text{subg-tend}}$) and RF-diff (d-f, R^2 calculated for diffusivity) as evaluated on the training dataset (green) and validation dataset (red) for x8 and different hyperparameter values: (a,d) minimum samples in each leaf, (b,e) number of trees in the forest, and (c,f) number of training samples. The hyperparameters that are used for both RFs when implemented in SAM are 20 minimum samples in each leaf, 10 trees in the forest and 5,000,000 training samples for the x4, x8, and x16 simulations. The hyperparameters that are used for both RFs in the x32 simulations are 7 minimum samples in each leaf, 10 trees in the forest and 1,969,020 training samples.

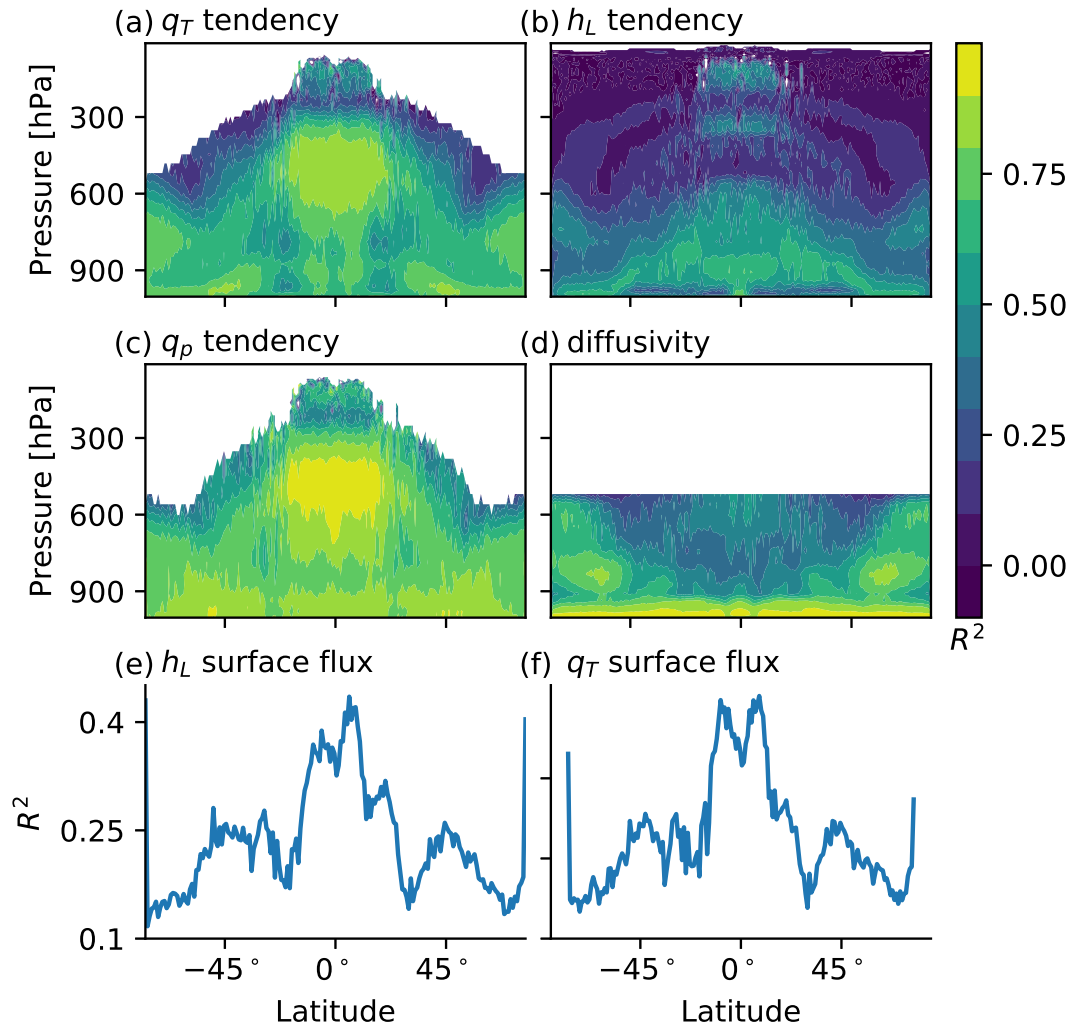


Figure S2: Coefficient of determination (R^2) for offline performance at x8: (a) subgrid tendency of q_T , (b) subgrid tendency of h_L , (c) subgrid tendency of q_p , (d) turbulent diffusivity, (e) subgrid surface flux of h_L , and (f) subgrid surface flux of q_T . Results are based on the samples from the test dataset. R^2 is only shown where the variance is at least 0.1% of the mean variance over all latitudes and levels.

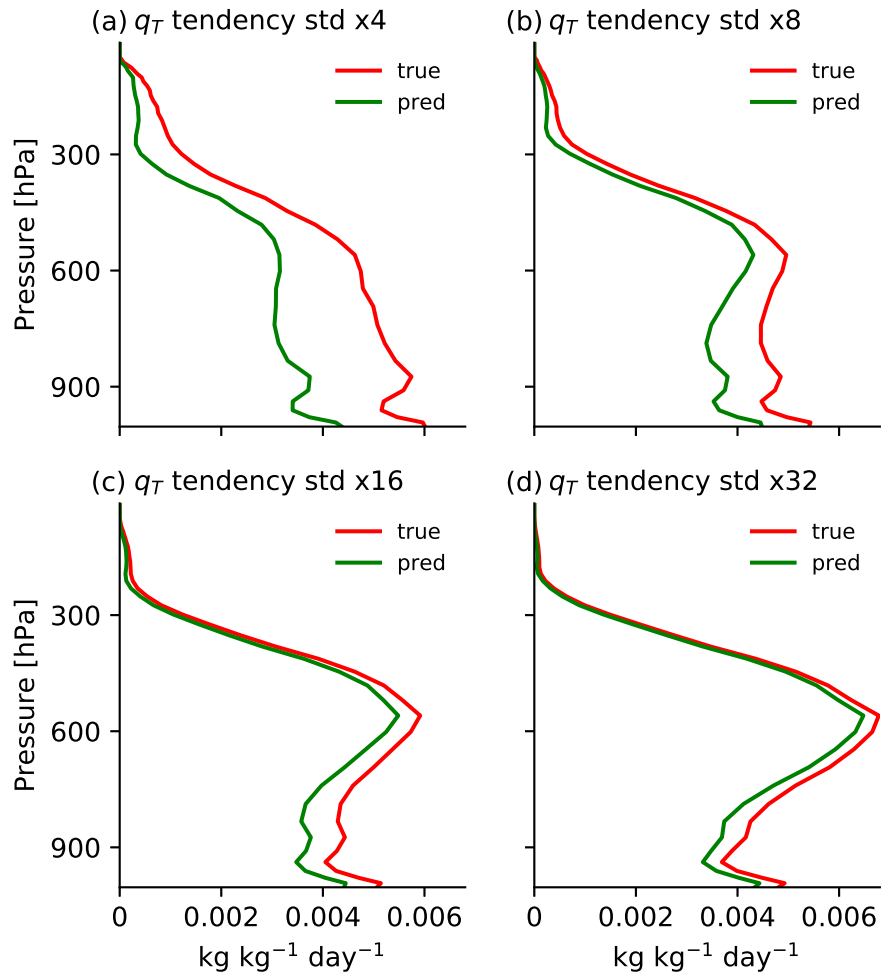


Figure S3: Vertical profiles of the standard deviation of the true (red) and RF-predicted (green) values of subgrid tendency of q_T for different coarse-graining factors (a) x4, (b) x8, (c) x16, and (d) x32. Results are evaluated based on the test dataset.

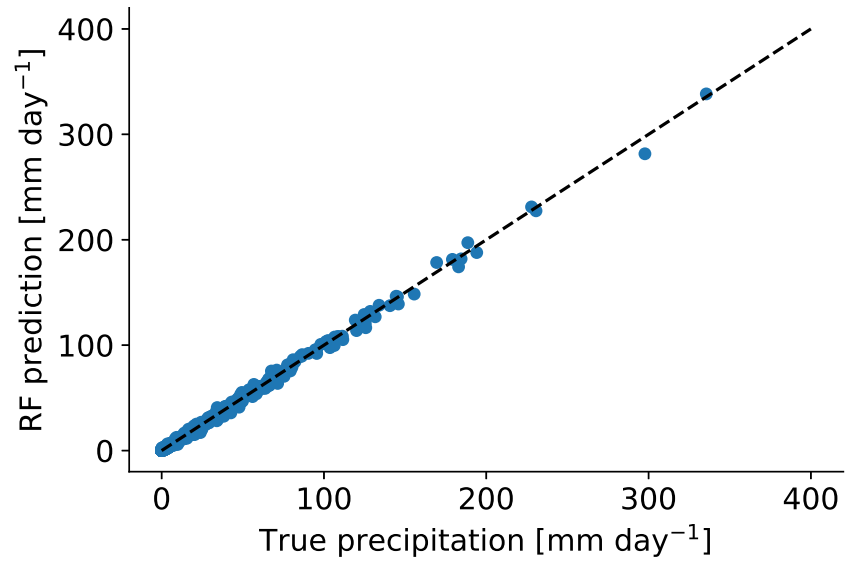


Figure S4: Scatter plot of true instantaneous surface precipitation coarse-grained to x8 versus the RF prediction. The RF-predicted precipitation is calculated as the sum of the resolved precipitation and the subgrid correction. A random subset of 10,000 samples from the test set are shown for clarity. The black dashed line is the one-to-one line. We verified that the RF prediction gives non-negative precipitation values for all the 972,360 test samples.

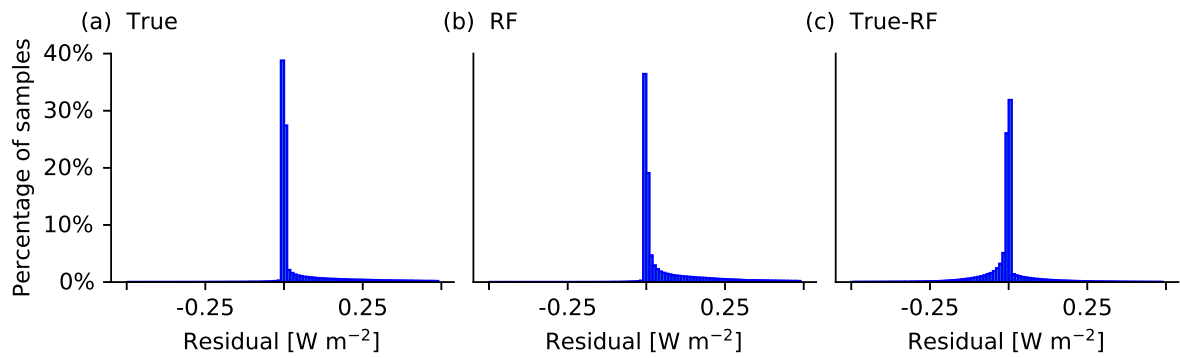


Figure S5: Distribution of energy-conservation residuals (equation S8) applied to samples in the test dataset at x8 for the (a) true subgrid tendencies, (b) predicted subgrid tendencies, and (c) the difference between the true and RF-predicted subgrid tendencies. The bin size is 0.01Wm^{-2} .

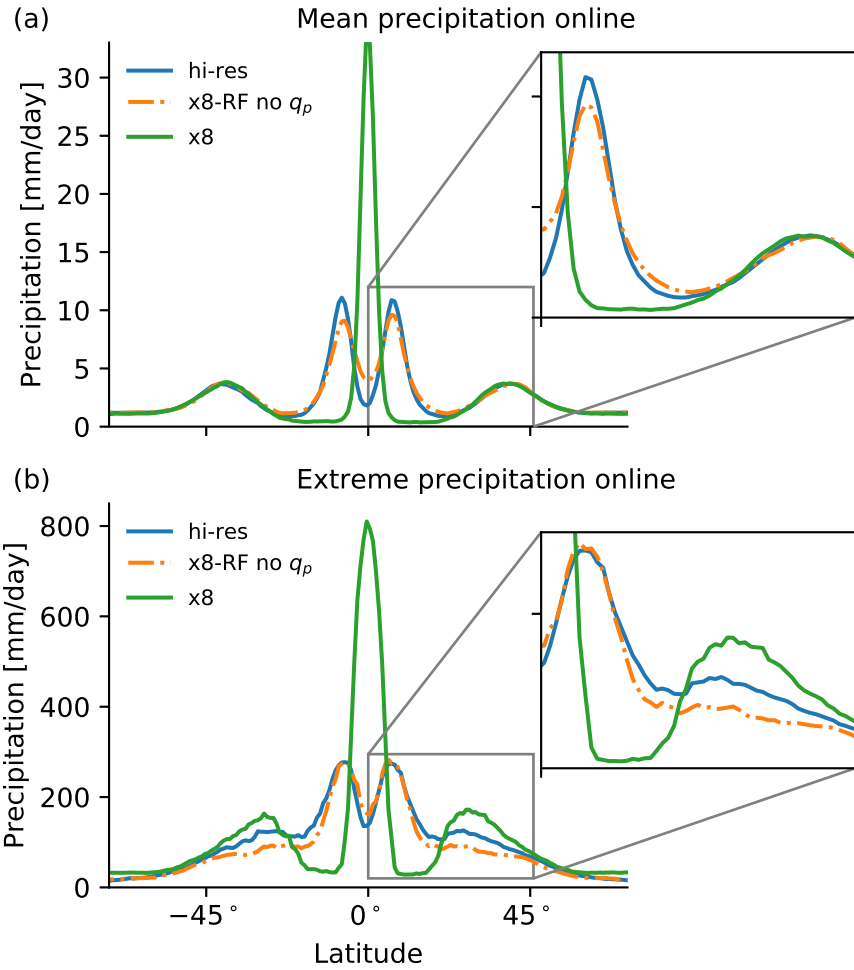


Figure S6: Mean and extreme precipitation as a function of latitude for simulations with the alternative RF-parameterization that does not use the precipitating water as a variable: (a) mean precipitation and (b) 99.9th percentile of 3-hour precipitation at each latitude from the hi-res simulation (blue), x8-RF simulation without q_p (orange), and x8 simulation (green).

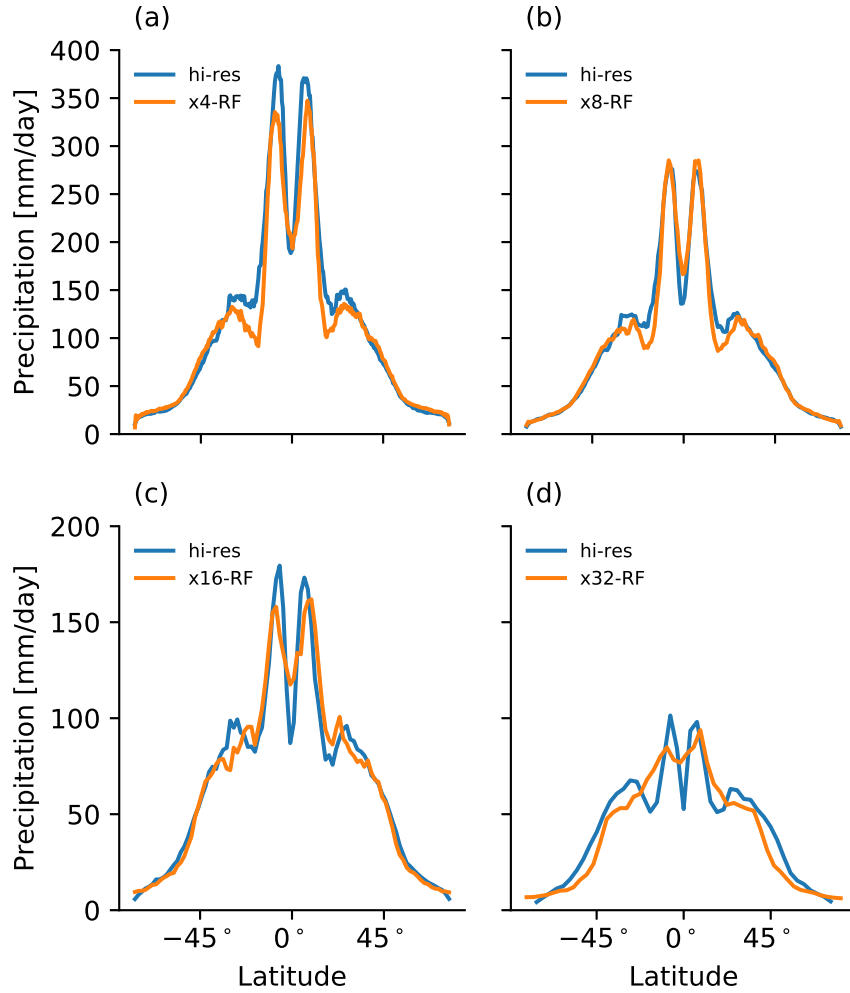


Figure S7: Extreme precipitation as measured by the 99.9th percentile of 3-hourly precipitation as a function of latitude for simulations with different horizontal grid spacing: (a) x4, (b) x8, (c) x16 and (d) x32. Shown are the results for the high-resolution simulation (blue) and the coarse-resolution simulation with the RF parameterization (orange). The precipitation rates for the high resolution simulation have been coarse-grained to the appropriate grid spacing prior to calculating the percentiles [14].

	$q_T^{subg-tend}$	$h_L^{subg-tend}$	$q_p^{subg-tend}$	diffusivity	$q_T^{surf-flux}$	$h_L^{surf-flux}$
x4	0.56	0.31	0.76	0.72	0.30	0.26
x8	0.80	0.48	0.88	0.84	0.38	0.34
x16	0.90	0.64	0.93	0.91	0.48	0.44
x32	0.95	0.75	0.96	0.96	0.72	0.67

Table S1: Offline performance as measured by R^2 for different coarse-graining factors and different outputs of the RFs. For the tendencies and turbulent diffusivity, all levels used are included when calculating R^2 . All results are based on the test dataset.

	x8-RF	x8
Eddy kinetic energy	0.97	0.87
Zonal wind	0.97	0.84
Meridional wind	0.87	-0.14
Non-precipitating water	0.99	0.97

Table S2: Online performance as measured by R^2 of zonal- and time-mean variables for the coarse-resolution simulations with the RF parameterization (x8-RF) and without the RF parameterization (x8) as compared to the target hi-res simulation. Results are given for the eddy kinetic energy, the zonal wind (u), the meridional wind (v) and the non-precipitating water mixing ratio (q_T). The eddy kinetic energy is defined with respect to the zonal and time mean.